Analysis of the Dominant Signal Component of the Air-Ground Channel Based on Measurement Data at C-Band

Daniel M. Mielke, Nicolas Schneckenburger, *Member, IEEE*, Uwe-Carsten Fiebig, *Member, IEEE*, Michael Walter, *Senior Member, IEEE*, Miguel A. Bellido-Manganell

***Abstract*—Operating remotely piloted aircraft is not imaginable without a continuous data exchange between the air vehicle and the remote pilot. This data exchange requires reliable data links. One approach for such a data link discussed in the community is a terrestrial system deployed in C-band. A good knowledge of the physical conditions of the communication channel, in this case the air-ground/ground-air channel, is indispensable for the development of wireless data links. Therefore we carried out a 50 MHz bandwidth channel sounding campaign with a terrestrial transmitter and an airborne receiver.**

In this paper we give a detailed description of our campaign setup and the processing of the collected data. The campaign covered several flight scenarios, such as take-off, taxiing, and multiple en-route maneuvers. We furthermore present results on the received power and the amplitude distribution of the dominant component of the received signal for the different flight scenarios. We observed significant drops in reception power during certain maneuvers that need to be considered in the design process of a data link for unmanned aviation. Additionally, we show that the amplitude distribution follows the distributions commonly used in statistical channel modeling of wireless channels to some extent. We finally present parameter sets for multiple flight scenarios for scaling the amplitude distributions to allow a statistical channel modeling of the reception power of the first resolvable signal path.

I. Introduction

MORE and more Unmanned Aircraft (UAs) are expected to enter the skies both in the controlled and uncontrolled airspace during the next years. For example, the market for UAs in the European Union is expected to make up to 10 % of the European aviation market [1] during the next ten years. The anticipated fields of application are transportation or other logistic tasks, as well as surveillance, exploration, and tasks in the agronomy.

It is ruled out, that these UAs will operate completely autonomously and non-cooperatively. Furthermore, there is also the UA subset of Remotely Piloted Aircraft (RPAS) that do not operate autonomously and require, as the name indicates, a remote pilot. Hence, there is a need for a reliable communication system between the UAs and a central controlling instance and a remote pilot.

In the field of manned aviation, most communication is still performed using analogue voice radio. However, more advanced technologies have been applied during the last years, e. g. Aircraft Communications Addressing and Reporting System (ACARS) or Very High Frequency Data Link (VDL). While these systems are designed as a complement to the still indispensable analogue voice radio, new developments are on their way to provide a more modern communication system. The terrestrial solution is the L-Band Digital Aeronautical Communication System (LDACS) [2], [3]. It provides both voice and data communication, e. g. for the exchange of additional information like flight tracks and telemetric data. Nonetheless, it has not been designed to fulfill the requirements for a Control and Non Payload Communications (CNPC) link for UAs as identified in [4], [5].

The C-Band Digital Aeronautical Communication System (CDACS) is an approach for such a system. It is designed for the frequency range of 5030 MHz and 5091 MHz that is intended for Command and Control (C2) links for UAs [6]. First concepts have been presented in [7], [8]. So far, common channel models have been parameterized based on literature for the CDACS design, as the knowledge of the physical properties of the wireless communication channel is crucial [9]. The data base for these models was taken from literature, e. g. the model used during the development of Aeronautical Mobile Airport Communication System (AeroMACS) as described in [10] among others. A common procedure to gain knowledge on the communication channel – in case of CDACS, this is the terrestrial ground-air channel in C-band – are channel measurements, often called channel sounding. Based on these measurements, a channel model is developed that is then used to design, evaluate and optimize the wireless waveform. Channel sounding campaigns for the C-band terrestrial ground-air channel have already been performed. The results of a large L- and C-band measurement campaign have been presented in [11], [12], [13], [14]: While [11] presents the general campaign setup and findings on the channel behavior in over-water scenarios, [12] focuses on the wave propagation in hilly and mountainous terrain. Suburban and near-urban scenarios have been covered in [13]. Finally, the effect of airframe shadowing during flight has been investigated and modeled in [14].

The German Aerospace Center (DLR) performed another measurement campaign to get a better understanding of the C-band air-ground/ground-air channel, especially during flight scenarios not covered by previous campaigns. For example, our campaign mostly contained flight tracks with circular

D. M. Mielke, U.-C. Fiebig, M. Walter, and M. A. Bellido-Manganell are with the German Aerospace Center (DLR), Institute of Communications and Navigation, 82234 Wessling, Germany (e-mail: {daniel.mielke, uwe-carsten.fiebig, m.walter, miguel.bellidomanganell}@dlr.de), N. Schneckenburger is with ... (email: nicolas.schneckenburger@gmail.com)

and square shaped flight patterns and the transmitter in the center of the respective pattern. We furthermore flew certain maneuvers close to the transmitter located at a regional airport to investigate the channel behavior in critical situations. The campaign was planned with the experience gained during previous flight measurement campaigns like [15]. A high level overview of the new measurement campaign has already been published in [16].

This paper aims to provide considerably more details on the campaign setup and the data processing. Furthermore, we provide results on the reception of the dominant component received at the transmitter, often misleadingly called the Line of Sight (LOS) component, for different flight scenarios. The dominant component typically contains the actual LOS signal among other signal components that cannot be resolved from the LOS signal due to a limited resolution. Typical examples for non-resolvable components are the signal reflected off the ground and signals reflected or scattered in the vicinity of the transmitter or receiver, respectively.

The sequel of this paper is structured as follows: We describe the overall channel sounding procedure and the used channel sounding waveform in Section II. The hardware setup is presented in Section III. The processing of the collected data of the campaign is explained in Section IV, while the flight routes and performed flight maneuvers are described in Section V. Results covering the received power of the dominant component are presented in Section VI; the distribution of the received amplitudes are presented in Section VII.

II. Channel Sounding

The motivation of channel sounding has been described in the previous section. But what is the *channel* that is actually sounded? Obviously, the *desired* channel that we are interested in is *only the wireless channel* between the transmitting and the receiving antennas. However, it is impossible to *only* measure this channel, since a number of hardware effects influence the signals on both the transmitting and the receiving side. An often applied strategy of minimizing the impact of these effects onto the final channel model is to perform reference measurements. They allow isolating and compensating these hardware effects by appropriate signal processing. Details on how this compensation is applied are given in Section IV.

A. Center Frequency

Although the anticipated frequency band for a C2 link is $5.030\,\mathrm{GHz}$ to $5.091\,\mathrm{GHz}$, the center frequency f_c used in this campaign is $5.200\,\mathrm{GHz}$. This decision was made due to hardware availability; however, the authors do not expect significant channel deviations between these two bands.

B. Waveform Design

The waveform used in the campaign is a so called multi-tone signal. Multi-tone signals are a popular type of waveform; technologies like Orthogonal Frequency Division Multiplexing (OFDM) are a well-known subclass of these type of signals. Furthermore, multi-tone signals are popular in channel-sounding, however, they suffer from a high Peak-to-Average Power Ratio (PAPR). In communications, a signal with a high PAPR usually requires the High Power Amplifier (HPA) to operate at a significant back-off resulting in an imperfect operating point to avoid distortions or even hardware damage.

The channel sounding signal $\boldsymbol{s}_\mathrm{CS}$ used in the campaign is generated in two steps:

- First, a basic signal is generated according to:

$$\boldsymbol{s}_{\mathrm{CS},0} = \mathfrak{IFFT}_N\{[0, ..., X_{n-1}, X_n, X_{n+1}, ..., 0]\} \quad (1)$$

  where $\mathfrak{IFFT}\{.\}$ denotes the inverse Fast Fourier Transform (FFT) and the vector elements have the same absolute value and phases distributed as Newman Phases [17] according to

$$X_n = e^{j\pi\frac{(n-1)^2}{N}}, \quad \forall\ n \in \left\{-\frac{N}{2} + N_\mathrm{G} + 1, ..., \frac{N}{2} - N_\mathrm{G} \middle| n \neq 0\right\}. \quad (2)$$

  The FFT-length (thus the overall amount of subcarriers) is set to $N = 2048$, while $N_\mathrm{G} = 5$ guard carriers are used to provide guard bands for the expected Doppler shifts.
- In a second step, the PAPR is reduced by iteratively applying clipping and filtering:

$$\boldsymbol{s}_{\mathrm{CS},k} = \mathrm{Filt}\big\{\mathrm{Clip}_a\{\boldsymbol{s}_{\mathrm{CS},k-1}\}\big\}, \forall\ 0 < k \leq K, \quad (3)$$

  where $\mathrm{Filt}\{...\}$ denotes the application of an ideal Band-Pass (BP) filter, $a = 0.95$ defines the clipping limit and $K = 80\,000$ defines the iteration limit. The last step of the generation sets $\boldsymbol{s}_\mathrm{CS} = \boldsymbol{s}_{\mathrm{CS},K}$ and the signal gets upsampled by a factor of $f_\mathrm{up} = 2$: $\boldsymbol{s}_\mathrm{CS,up} = \mathrm{UPS}_{f_\mathrm{up}}\{\boldsymbol{s}_\mathrm{CS}\}$. The upsampling is necessary because of the internal filter design of the Arbitrary Waveform Generator (AWG) used to play the generated signal.

The overall bandwidth of the resulting signal sampled at $100\,\mathrm{MHz}$ is $49.78\,\mathrm{MHz}$ resulting in a spacial resolution of $\Delta r_\mathrm{min} \approx 5.994\,\mathrm{m}$. This is the maximum bandwidth achievable with the available hardware.

The signal's PAPR is calculated according to

$$\mathrm{PAPR}_\mathrm{dB}(\boldsymbol{x}) = 10\log_{10}\left\{\frac{\max\{\boldsymbol{x}\ \boldsymbol{x}^*\}}{\mathrm{E}\{\boldsymbol{x}\ \boldsymbol{x}^*\}}\right\}, \quad (4)$$

where $\boldsymbol{x}^*$ denotes the complex conjugate of $\boldsymbol{x}$. The PAPR of the channel sounding signal has been determined to be $\mathrm{PAPR}_\mathrm{dB}(\boldsymbol{s}_\mathrm{CS,up}) \approx 0.285\,\mathrm{dB}$.

The time-discrete signal $\boldsymbol{s}_\mathrm{CS,up}$ is replayed in an infinite loop and is converted into the time-continuous transmission signal $s_\mathrm{Tx}(t)$ according to

$$\begin{aligned} s_\mathrm{Tx}(t) &= \sum_{n=-\infty}^{\infty} \boldsymbol{s}_\mathrm{CS,up}[\underset{Nf_\mathrm{up}}{\mathrm{mod}}(n)] \cdot g_\mathrm{Tx}\left(t - \frac{n}{f_\mathrm{SR} f_\mathrm{up}}\right) \\ &= \sum_{n=-\infty}^{\infty} \boldsymbol{s}_\mathrm{CS}[\underset{N}{\mathrm{mod}}(n)] \cdot g_\mathrm{Tx}\left(t - \frac{n}{f_\mathrm{SR}}\right), \end{aligned} \quad (5)$$

where $\underset{D}{\mathrm{mod}}(a)$ denotes the modulo operation on a to basis D and $g_\mathrm{Tx}(t)$ denotes the transmission filter, i.e. the characteristics of the AWG's Digital-to-Analog Converter (DAC).

TABLE I
PARAMETERS OF THE CHANNEL SOUNDING SEQUENCE

Description	Symbol	Value	Unit
Sample Rate	f_{SR}	50	MHz
Sequence Length	N	2048	Smpl
Sequence Length	T_{CSS}	40.96	µs
Carrier Frequency	f_c	5.200	GHz
Wave Length	λ_c	5.764	cm
Sequences per File	-	48 000	-

Fig. 1. a) Position of the transmitting antenna on the rooftop of the building of IKN. b) The portable Ground Station.

III. HARDWARE SETUP

The campaign involved one ground-based transmitting station – in the following: Ground Station (GS) – and one receiving station located onboard a Dassault Falcon 20E aircraft – in the following: Airborne Station (AS).

A. Ground Station

Since the reference measurement procedure described in Section III-C requires the operation of the GS at two different locations, the GS is designed as a portable platform as shown in Fig. 1b). Its block diagram is presented in Fig. 2. All devices are explained in the following.

1) Rubidium (Rb)-Clock and GNSS Receiver: Together, the Rb-clock[1] and the Global Navigation Satellite System (GNSS) receiver[2] form a GNSS-disciplined oscillator and built the time base of the GS. This is a common approach to benefit from both the short-term clock-stability of Rb-clocks and the long-term clock-stability of the GNSS system at the same time. GNSS data is logged during all measurements and converted into the common RINEX data format afterwards.

2) Arbitrary Waveform Generator (AWG): The pre-generated channel sounding signal $\boldsymbol{s}_{CS}$ is loaded into the AWG[3] and played at 100 MHz in an infinite loop during measurements. The AWG uses the 10 MHz reference signal of the Rb-clock and its average output power is set to -5.5 dBm.

[1]Spectratime LNRCLOK-1500
[2]JAVAD Delta3
[3]Rohde & Schwarz SMBV100

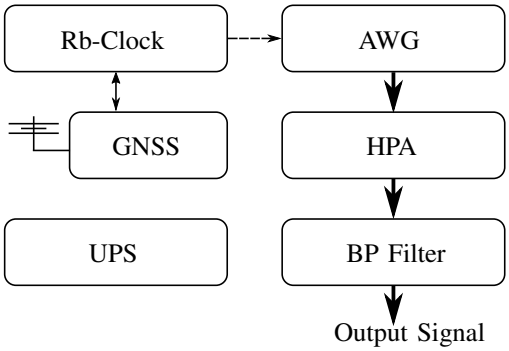

Fig. 2. Block diagram of the Ground Station. Bold arrows denote the flow of the channel sounding signal, dashed arrows denote the 10 MHz reference signal, other arrows denote data lines. All devices are explained in detail in Section III-A.

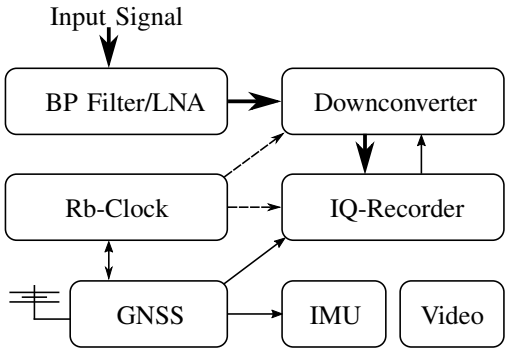

Fig. 3. Block diagram of the Airborne Station. Bold arrows denote the flow of the channel sounding signal, dashed arrows denote the 10 MHz reference signal, other arrows denote data lines. All devices are explained in detail in Section III-B.

3) High Power Amplifier (HPA) and Filter: The HPA[4] amplifies the AWG's output signal by an average gain of 53.5 dB. An additional BP filter (center frequency at 5.2 GHz, pass-band bandwidth of ∼400 MHz) is connected to the output of the HPA to reduce out-of-band radiation. Due to the losses implemented by the BP filter, cables, and connectors, the average output power of the channel sounding signal coming out of the filter is $P_{out} \approx 47.5$ dBm. Thus, the HPA is running with a backoff w. r. t. its 1 dB Gain Compression Point of $P_{1dB\text{-}GCP} = 49.5$ dBm to avoid nonlinear distortions.

4) Uninterruptible Power Supply (UPS): All active devices of the GS, except for the HPA, are connected to the UPS[5] to allow a mobile operation of the GS for about 12 min.

5) Transmitting Antenna: During the measurement flights, a transmitting antenna was used having an average gain of $G_{Tx} \approx 5$ dBi. The antenna characteristics are part of the campaign results. Vertical polarization is used, as this is the common polarization in other aeronautical air-ground communication systems [18], [19].

B. Airborne Station

The receiving equipment onboard the Falcon aircraft was as follows.

[4]Microwave Amps AM60 Series
[5]Eaton 9130

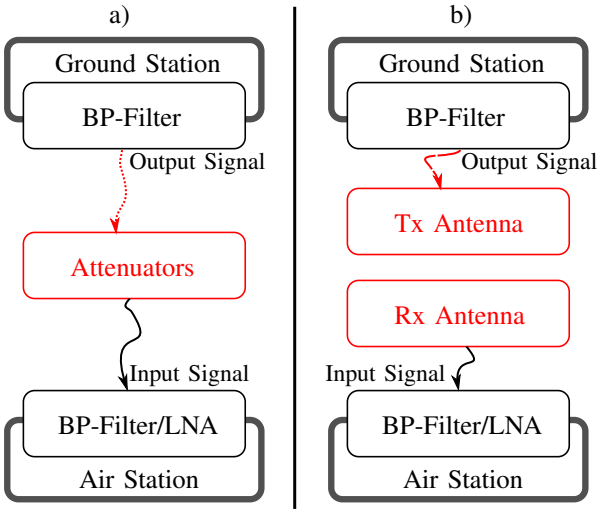

Fig. 4. Sketch describing the setup during a) the reference measurement and b) the actual measurement flight. Red lines depict hardware whose effects on the radio signal are not neutralized by taking the reference measurement into account during signal processing.

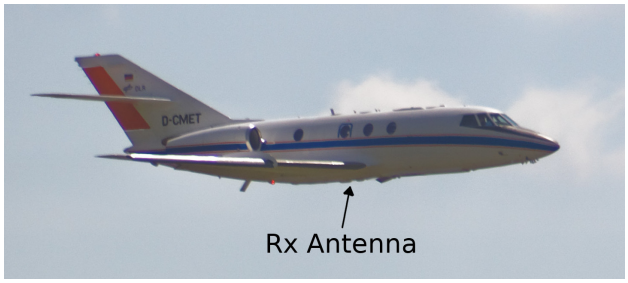

Fig. 5. Position of the receiving antenna on the bottom of the Falcon aircraft.

1) Rb-Clock and GNSS Receiver: Similar to the GS, these devices form a GNSS-disciplined oscillator to provide a stable clock source through a 10 MHz reference signal. GNSS data is logged during all measurements and converted into the common RINEX data format afterwards.

2) BP Filter and Low Noise Amplifier (LNA): The incoming signal is filtered and amplified by a two-stage LNA and corresponding BP filters. The overall gain including cable and filter losses is ∼14.1 dB.

3) Downconverter: The pre-amplified signal is converted from the incoming carrier frequency $f_c = 5.2\,\mathrm{GHz}$ to an intermediate frequency of $f_{IM} = 80\,\mathrm{MHz}$. The mixer inside the device uses the reference signal of the GNSS-disciplined oscillator as a clock basis. The downconverter is equipped with a variable gain G_{DC} that is set by the software of the IQ-recorder via a serial interface.

4) IQ-Recorder: The IQ-recorder[6] records the incoming signal at a sample rate of $f_{SR} = 50\,\mathrm{MHz}$ with a resolution of 14 bit for each the real and imaginary part of a sample. Sets of 98 304 kSmpl are stored in a binary file together with a header including the current GNSS-timestamp, the current sample counter value ρ, and the current value of the gain control G_{DC} of the downconverter. The resulting data stream of more than $175\,\mathrm{MB/s}$ motivates the usage of a RAID[7], which is considered as part of the "IQ-Recorder" block in Fig. 3 for the sake of simplicity. The IQ-Recorder uses the reference signal of the GNSS-disciplined oscillator as a clock basis.

5) Video and Inertial Measurement Unit (IMU): An IMU[8] is used to record data on the orientation of the aircraft. The data is logged including GNSS-timestamps. For documentation, a video camera is filming all flights through the window over the left wing of the Falcon aircraft.

6) Receiving Antenna: A vertical polarized receiving antenna is used. According to the manufacturer's data-sheet, it provides an omnidirectional antenna pattern with an antenna gain of $G_{Rx} \approx 4\,\mathrm{dBi}$. A more precise description of the receiving antenna's pattern is not available. The receiving antenna is mounted at the bottom of the aircraft as shown in Figs. 5 and 6. This location is determined by the architecture of the research aircraft.

[6]National Instruments PXI Series, Windows 7 with LabView

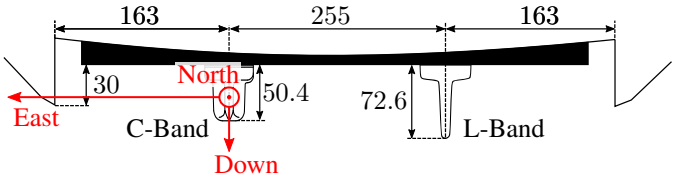

Fig. 6. Front view sketch of the receiving antenna mounted at the bottom of the aircraft, not true to scale. The C-Band antenna is used to receive the channel sounding data, the L-Band antenna is used for another mission. All measurements are given in mm. The axes of the receiver centered North-East-Down (NED) coordinate system are marked in red, see Appendix C for more information.

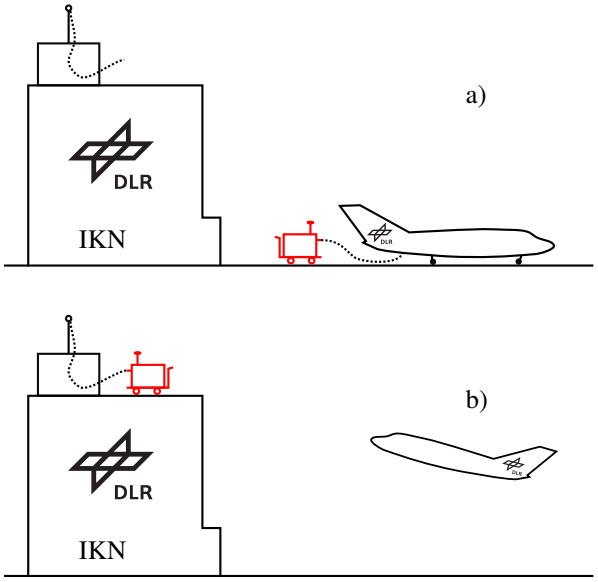

Fig. 7. Schema of the two locations of the Ground Station (red). a) The GS is located next to the aircraft on the apron for calibration purpose before and after each flight. b) The GS is located in its transmission location on top of the IKN building providing a similar setting as it was located on an airport tower.

C. Measurement Procedure

Each measurement flight consisted of the following steps:

[7]National Instruments HDD8265
[8]xSens MTi-100 Series

1) Pre-Flight Reference Measurement: The aircraft is on the apron with active Auxiliary Power Unit (APU). The receiver station onboard the aircraft runs on the aircraft's APU power; IQ-sample recording is prepared but paused. The GS is located next to the aircraft on the apron and is connected to the local power supply network as shown in Fig. 4a) and Fig. 7a). The Rb-clocks of the GS and the AS have been synchronized via cable. The filter output is connected to the antenna cable of the receiving antenna using a cascade of attenuators. The attenuators provide an overall attenuation of $A_{\mathrm{dB,ref}} = 90\,\mathrm{dB}$, corresponding to a Free Space Path Loss (FSPL) of $\sim 0.15\,\mathrm{km}$ for the given f_c. The GS starts transmitting the channel sounding signal, the AS starts the IQ-sample recording for about $10\,\mathrm{s}$.

2) Moving the Ground Station: The GS is moved from the apron into its transmission location on the rooftop of the institute's building. While the HPA is switched off during the relocation, the GNSS-receiver, the Rb-clock, and the AWG are running on the UPS. Once the transmitting location is reached (see Fig. 7b)), the station is connected to the local power supply network. The filter output is connected to the antenna cable and the HPA is switched on: The transmission of the channel sounding signal is started.

3) Actual Measurement Flight: The receiving antenna of the aircraft is connected to the AS and IQ-sample recording is started in the AS. The aircraft starts taxiing and takes-off. Once the aircraft reached its parking position on the apron after the flight, the recording of the IQ-samples is paused again; all AS devices are kept running on APU power.

4) Moving the Ground Station: The GS terminates its transmission by shutting down the HPA. The GS is disconnected from the power supply network and moved back from its transmission location to the apron where the aircraft is waiting. Again, the HPA is switched off while the GNSS-receiver, the Rb-clock, and the AWG are running on the UPS.

5) Post-Flight Reference Measurement: The same procedure as during the pre-flight reference measurement is performed again after each flight. Both measurements are compared during post-processing to get a better understanding of possible hardware drifts during the measurement flight.

IV. Data Processing

A. Received Signal

The signal at the receiver can be described as

$$s_{\mathrm{Rx}}(t) = s_{\mathrm{Tx}}(t) * h(t) + n(t), \tag{6}$$

where $*$ denotes the convolution, $h(t)$ describes the (unknown) channel impulse response and $n(t)$ describes white Gaussian noise.

The time-discrete signal $\boldsymbol{s}_{\mathrm{Rx}} = [s_{\mathrm{Rx},0}, s_{\mathrm{Rx},1}, ...]$ is created by sampling according to

$$s_{\mathrm{Rx},k} = \left(s_{\mathrm{Rx}}(t) * g_{\mathrm{Rx}}(t)\right)\left(\frac{k}{f_{\mathrm{SR}}}\right), \quad k \in \mathbb{N}, \tag{7}$$

where $g_{\mathrm{Rx}}(t)$ is the filter of the Analog-to-Digital Converter and f_{SR} denotes the sample rate.

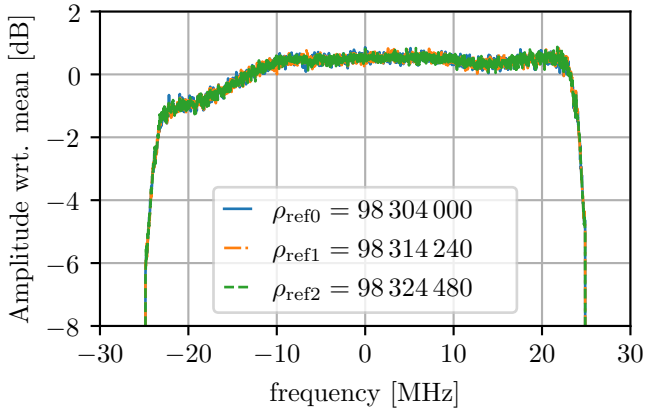

Fig. 8. Logarithmic spectra of three arbitrarily chosen reference signals. The frequency responses of the different reference signals show only very small deviations for several time instants.

B. Channel Sounding Signal Processing Concept

The basic idea of the processing is to compare the reference measurement signal $\boldsymbol{s}_{\mathrm{Rx,ref}}$ with the signal received during flight $\boldsymbol{s}_{\mathrm{Rx}}$ as suggested in [20]. Before the received data of a flight can be processed, the reference signal recorded before (or after) the corresponding flight needs to be loaded.

C. Extracting the Reference Signal

From the properties of the transmission signal (5) and the recording sample rate it follows that a vector of $N = 2048$ samples of the received IQ data is guaranteed to contain *exactly* one (circularly shifted) instance of the channel sounding signal $\boldsymbol{s}_{\mathrm{SC}}$. Thus, an arbitrary vector of length N can be chosen from the reference measurement data starting at sample number ρ_{ref} as the reference signal used for evaluation:

$$\boldsymbol{x}_{\mathrm{ref}} = \boldsymbol{s}_{\mathrm{Rx}}[\rho_{\mathrm{ref}}, ..., \rho_{\mathrm{ref}} + N - 1]. \tag{8}$$

The logarithmic spectra of three different $\boldsymbol{x}_{\mathrm{ref}\{0,1,2\}}$ with arbitrarily chosen start sample numbers $\rho_{\mathrm{ref}\{0,1,2\}}$ are plotted in Fig. 8. Apparently, the deviations between these three different instances are extremely small and are therefore considered as negligible.[9] Thus, the actual value of ρ_{ref} is free of choice; however, the actual value of ρ_{ref} is later required to determine the time shift when comparing the extracted reference signal with the measurement signal. We define T_{ref} as the time instance of the recording of ρ_{ref}.

D. Hardware Effects

The concept presented in Section IV-B helps reducing the general problem of channel sounding described in Section II by neutralizing most of the hardware effects onto the measurement signal. However, only hardware that is part of *both* the reference measurement *and* the actual channel sounding measurement is affected by this neutralization. This was *not* the case for the following items (also highlighted in Fig. 4):

[9]This statement implies the assumption of a constant frequency response of the hardware during one measurement flight.

1) Cable from the BP filter of the GS to the attenuators during the reference measurement a)
2) Cable from the BP filter of the GS to the transmitting antenna during the flight measurement b)
3) Attenuators used during the reference measurement a)
4) Transmitting and receiving antenna during flight measurement b).

The cables mentioned in 1) and 2), respectively, were of the same length of $8.40\,\mathrm{m}$ and of the same batch of the same manufacturer. Measurements with a Vector Network Analyzer showed that the relevant parameters (group delay, frequency response) do not show any significant variances; consequently, we consider the impaired effects of the different cables as negligible.

While the effects of the attenuators in 3) are also negligible, the antennas in 4) impair more severe effects and are part of the resulting measurement data. However, since most radio hardware (including all *active* devices and also $g_{\mathrm{Tx}}(t)$ and $g_{\mathrm{Rx}}(t)$) are part of both measurements, the most severe effects are fully compensated.

E. GNSS Data and Clock Drift

All GNSS data collected during the campaign was post-processed by the Precise Point Positioning (PPP) service of the Geodetic Survey of Natural Resources Canada using the SPARK algorithm. The PPP processing provides correction values to compensate clock drifts among other impairments.

The GNSS antenna is mounted at the top of the AS to allow a better reception of the GNSS signals during flight. However, the receiving antenna of the measurement signal is mounted at the bottom of the AS, thus in a different location from the GNSS antenna. The location of the GNSS antenna with respect to the receiving antenna is represented by the vector $\boldsymbol{e}_{\mathrm{GNSS}} \in \mathbb{R}^3$ given in the NED coordinate system as defined in Appendix C. A similar approach as described in [21] is used to map the measured GNSS data onto the actual receiving antenna's position by applying $\boldsymbol{e}_{\mathrm{GNSS}}$ and IMU data. This correction is consequently applied to all location based processing in both the NED system and the East-North-Up (ENU) system as defined in Appendix B.

The Rb-clocks of both the GS and the AS are subject to clock drifts. According to the manufacturer, the deployed Rb-clocks provide a typical clock stability of 1×10^{-12} in the applied GPS-locked operation mode. However, this value cannot be achieved in a real world scenario where the clocks are subject to vibrations, varying temperatures, and acceleration. The actual clock drifts are therefore expected to be higher than the value given by the manufacturer.

As an example, the clock drifts detected during PPP processing of the GNSS data of both clocks are plotted in Fig. 9. Apparently, the drift of the airborne Rb-clock is greater than the drift of the ground based clock. This difference can be explained by the unstable environmental conditions onboard the aircraft during flight. As the Rb-clocks are always synchronized directly (i.e. a few minutes) before the pre-flight reference measurement of the channel sounding signal as described in Section III-C1, the clock drifts during the reference measurement at T_{ref} are very low.

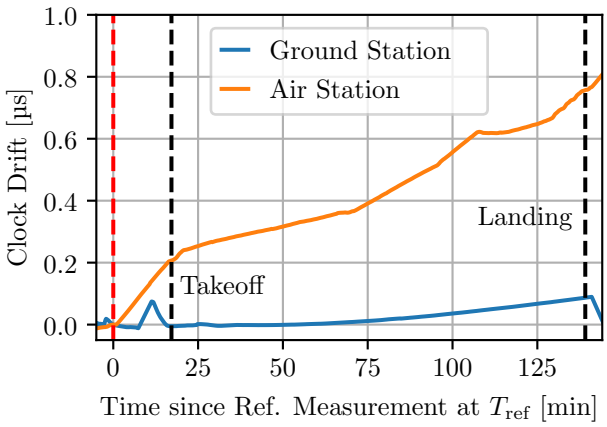

Fig. 9. Clock drifts of the Rb-clocks of the Ground Station and the Airborne Station during flight II. The x-axis represents the time since the pre-flight reference measurement of the channel sounding signal represented by T_{ref} as defined in Section IV-C. T_{ref} is marked by a horizontal dashed line in red; takeoff and landing are marked by horizontal dashed lines in black.

We explain the small peak of the drift of the GS clock between the pre-flight reference measurement and the takeoff with the relocation of the GS as described in Section III-C2.

The detected clock drifts need to be compensated during the processing of the channel sounding data. We denote the detected clock drifts of the GS and AS as $\tau_{\mathrm{GS}}(t)$ and $\tau_{\mathrm{AS}}(t)$, respectively. The overall clock drift compensation $\tau_{\mathrm{drift}}(t)$ at time instant t is computed according to

$$\tau_{\mathrm{drift}}(t) = \overbrace{\left(\tau_{\mathrm{AS}}(t) - \tau_{\mathrm{AS}}(T_{\mathrm{ref}})\right)}^{\text{Airborne Station}} - \overbrace{\left(\tau_{\mathrm{GS}}(t) - \tau_{\mathrm{GS}}(T_{\mathrm{ref}})\right)}^{\text{Ground Station}}. \quad (9)$$

V. Flight Overview

The campaign took place in July 2018 and consisted of four flights. All flights started and ended at the EDMO airport in Oberpfaffenhofen, Germany, thus close to the location of the GS. While the second flight was a long range flight with a LOS distance of up to $600\,\mathrm{km}$, the remaining flights took place in the area around EDMO ($< 60\,\mathrm{km}$). The flight routes of all flights are plotted in Fig. 10; the flight altitude (above mean sea level) is color coded. Flight dates and flight durations are presented in Table II.

All flights ended with a few go-arounds before the actual landing. In aviation, a go-around is initiated when a landing is aborted[10]. A go-around may happen during final approach "whenever landing conditions are not satisfactory" [22]. The go-around scenario, especially the part where the aircraft is above the runway, is dominated by strong multipath components besides the LOS path together with a comparatively high speed of the aircraft resulting in rapidly changing reflections, Doppler shifts, and Doppler spreads.

[10]"Go-around" is sometimes mistakenly used equivalently to "missed approach", although the latter term describes an aborted instrument approach.

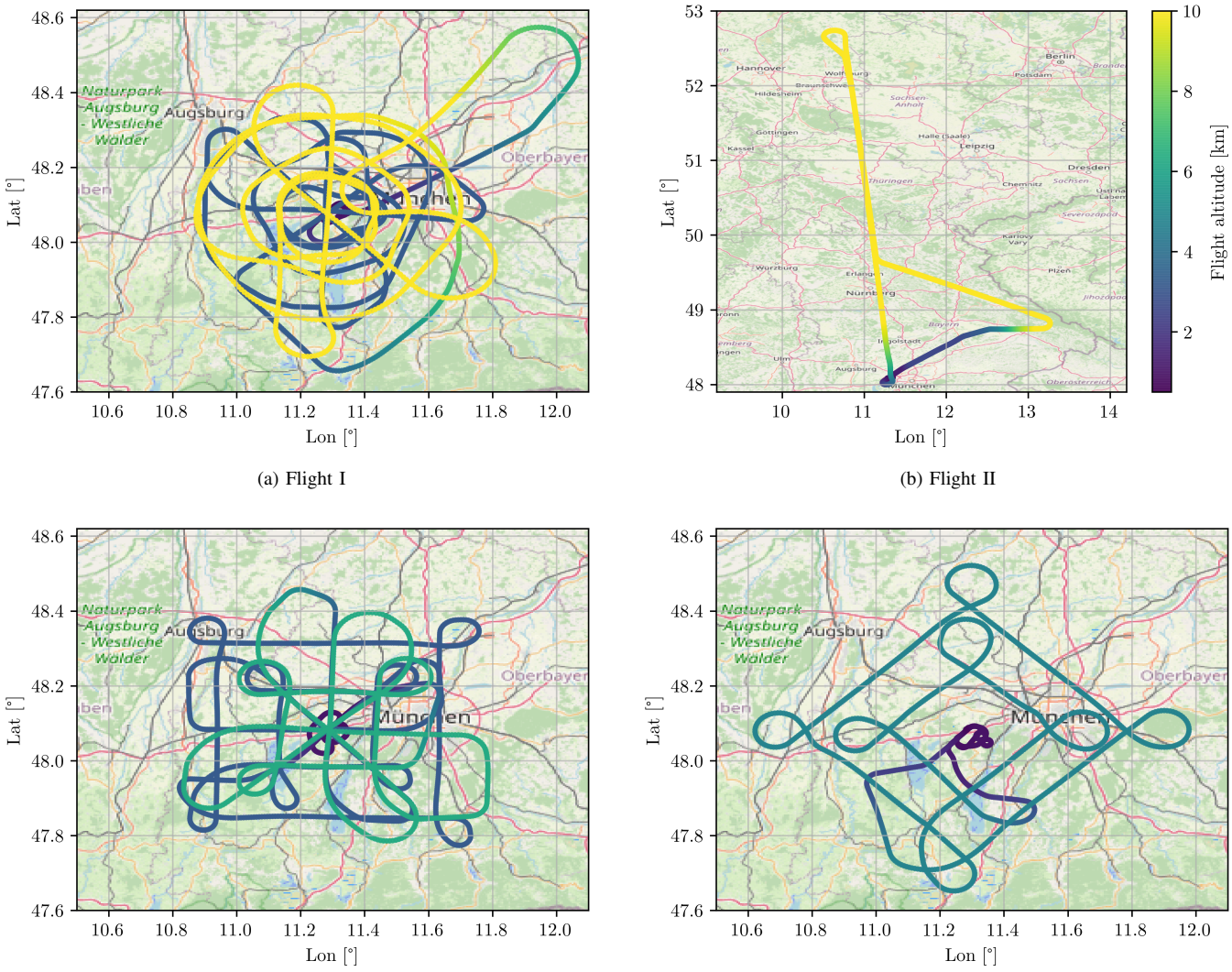

(a) Flight I

(b) Flight II

(c) Flight III

(d) Flight IV

Fig. 10. Flight routes of all flights. The flight altitude is color coded; the color key for all maps is given in Fig. 10b. Except for flight II, the routes were located in the area around the transmitter located at the EDMO airport in Oberpfaffenhofen, west of Munich.

TABLE II
BASIC FLIGHT STATISTICS

#	Date	Duration	# sequences
I	2018/07/09	3:25h	617.4×10^9
II	2018/07/10	2:10h	379.8×10^9
III	2018/07/10	3:10h	572.2×10^9
IV	2018/07/12	1:35h	281.8×10^9

Furthermore, maneuvers with rolling angles up to $\pm 50°$ were flown to investigate the effect of airframe shadowing during banking.

VI. POWER OF THE DOMINANT COMPONENT

We do not consider resolvable multipath propagation effects in this paper, rather we focus on the dominant signal component and evaluate its received power. This signal component is often misleadingly called the LOS signal. In fact, the actual LOS signal component is superimposed to multiple multipath components which cannot be resolved individually.

To calculate the power of this dominant component, the following processing is applied:

1) Blocks of B consecutive channel sounding sequence instances are taken from the received signal $\boldsymbol{s}_{\mathrm{Rx}}$, resulting in a vector of BN samples. Thus, the i-th block can be described as

$$\boldsymbol{c}_i = \mathfrak{F}^{-\nu_{\mathrm{LOS}}^{(i)}}_{-\tau_{\mathrm{LOS}}^{(i)}} \left\{ \boldsymbol{s}_{\mathrm{Rx}}[\rho_i, \ldots, \rho_i + BN] \right\}, \qquad (10)$$

with $\rho_i = iBN$, where $\tau_{\mathrm{LOS}}^{(i)}$ and $\nu_{\mathrm{LOS}}^{(i)}$ describe the LOS delay and LOS Doppler shift for block i, respectively, and $\mathfrak{F}^{\nu}_{\tau}\{.\}$ denotes a function shifting a signal by delay τ and frequency ν.

2) The coherent Power Delay Profile (PDP) is computed: $\boldsymbol{a}_i = \mathrm{PDP}_{\mathrm{coh}}^{f_{\mathrm{ups}}}(\boldsymbol{c}_i, \boldsymbol{x}_{\mathrm{ref}})$, where $f_{\mathrm{ups}} \in \mathbb{N}$ denotes the upsampling along the time axis and $\mathrm{PDP}_{\mathrm{coh}}^{f_{\mathrm{ups}}} : \mathbb{C}^{BN} \times \mathbb{C}^{N} \mapsto \mathbb{R}^{f_{\mathrm{ups}}N}$, see Appendix A.

3) The maximum of the PDP denotes the received power of the dominant signal component: $P'_{\mathrm{dB},i} := \max\{\boldsymbol{a}_i\}$.
4) As we are often interested in the received power without the effect of the FSPL, we furthermore define

$$P_{\mathrm{dB},i} := P'_{\mathrm{dB},i} - A_{\mathrm{dB,ref}} + \mathrm{FSPL}_i, \tag{11}$$

where $A_{\mathrm{dB,ref}}$ denotes the attenuation used when $\boldsymbol{x}_{\mathrm{ref}}$ was recorded during the reference measurement[11] and FSPL_i denotes the Free Space Path Loss for block i, estimated based on GNSS and IMU data.
We call $P_{\mathrm{dB},i}$ the calibrated received power of the dominant signal component of block i with respect to the FSPL.

The following results were computed with $B = 100$ if not denoted otherwise. This B corresponds to a block length of $4.096\,\mathrm{ms}$.

A. Banking Angle

The behavior of the received power computed according to (11) during strong banking is given in Fig. 11 providing the rolling angle (see Appendix C) on the y-axis. Raising the left wing and lowering the right wing indicates a positive rolling angle and vice versa.

By the time the given snapshot was recorded, the LOS distance was $4.6\,\mathrm{km}$ at a flight altitude of $1.01\,\mathrm{km}$. The aircraft passed the transmitter from southeast, heading northeast; thus, seen from aircraft, the transmitter was on the left side. Observing the transmitter's position given in NED spherical coordinates (see Appendix C) allows a precise declaration if airframe shadowing is present (LOS path not available) or not present (LOS path available). In Fig. 11, the background color indicates if the LOS path is available (light green color) or not available (light red color). The presence of the LOS path is determined evaluating the NED angles and the airframe architecture around the receiving antenna as sketched in Fig. 6. For the sake of completeness, we point out that no obstacles around the transmitter are blocking the LOS path for the observed period of time.

The presented rolling angle in Fig. 11 indicates, that the first bank ($0.2\,\mathrm{s}$ to $5.3\,\mathrm{s}$) leads to a loss of the LOS path since the received power P_{dB} drops down to $-30\,\mathrm{dB}$. This statement holds a comparison with the expected presence of the LOS path based on the NED angles. However, the figure shows that the dramatic drop in received power does not happen suddenly, but that a transition from strong reception to low reception is happening. We explain this observation by knife edge diffraction caused by the airframe, most likely the guide rails.

The second bank ($5.3\,\mathrm{s}$ to $11\,\mathrm{s}$) indicates a bank in the opposite direction, such that the receiving antenna has a direct view to the transmitter without any shadowing due to the airframe or similar. Consequently, the received power is up to $40\,\mathrm{dB}$ higher compared to the power received during the first bank.

[11] In (11) it is assumed the gain control settings G_{DC} used during the reference measurement and the recording of block i is already taken into account.

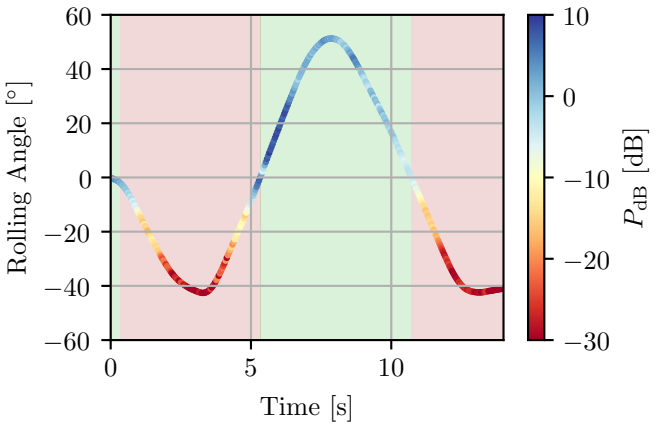

Fig. 11. Color coded received power during strong banking. The background color represents the presence of a LOS path that is determined from the polar angle of a receiver-centered North-East-Down (NED) coordinate system and the aircraft geometry, see Appendix C; red: "LOS path is blocked", green: "LOS path is present".

The third bank starting at $11\,\mathrm{s}$ shows the same behavior as the first bank.

B. Takeoff

The received power during takeoff is shown in Fig. 12. All flights started and ended at the EDMO airport, the starting direction was the same for all four flights (heading: south east). The position of the runway and the transmitter is shown in Fig. 15.

While P_{dB} is mostly in the range of $-2\,\mathrm{dB}$ to $4\,\mathrm{dB}$ as long as the aircraft is on the runway, one can observe an intense drop of up to $27\,\mathrm{dB}$ during takeoff and climbing. This observation applies to all four takeoffs in a very similar manner, however, the exact position of the strongest drops during climbing varies.

To understand the behavior of the received power, we have to recall that the receiving antenna is located at the bottom of the aircraft and that the aircraft is heading away from the transmitter during takeoff. This results in a complete block of the LOS path as long as the aircraft is climbing with a strong pitch angle in the given direction. Furthermore, no reflector close to the receiving antenna, which could result in a stronger received signal, is present. Nevertheless, the received power varies a bit and was observed to take on values as high as $-12\,\mathrm{dB}$. The moderate variations may be caused by signals reflected from buildings and obstacles located behind the runway when seen from the transmitter.

C. En-route (ENR)

Fig. 13 shows the received power during a part of flight II, i.e. the long range flight, vs. the LOS distance. The data shown in Fig. 13 was recorded during a northbound flight at an altitude of $9.3\,\mathrm{km}$, following a radial course away from the transmitter. One can observe a periodically changing received power within a dynamic range of $5\,\mathrm{dB}$. The period is in the

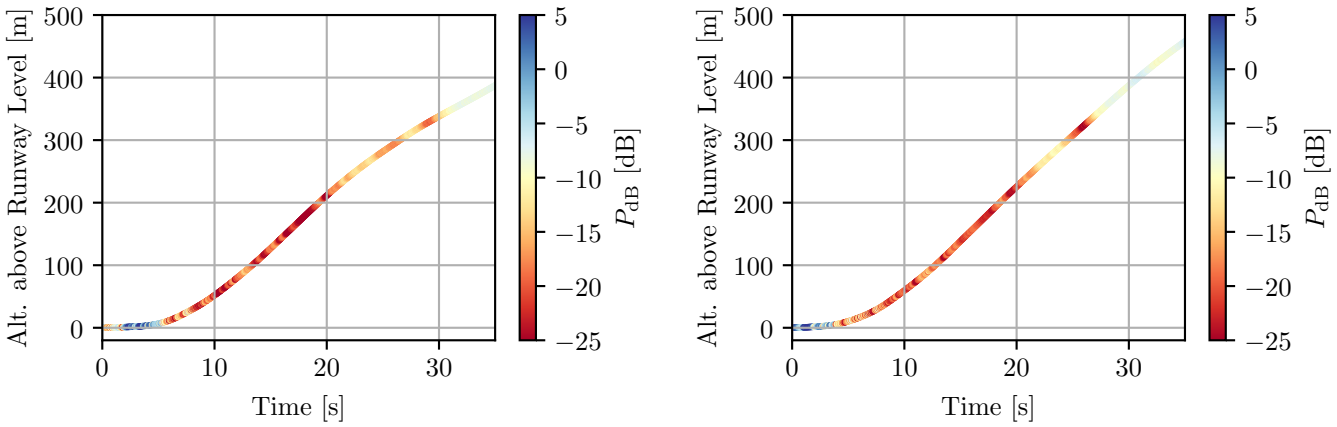

(a) Flight I

(b) Flight II

(c) Flight III

(d) Flight IV

Fig. 12. Color coded receiving power during take-off. The same runway with the same heading during takeoff was used for all flights.

range of 11 s, corresponding to a delta of about 1.5 km of LOS distance.

These oscillations can be interpreted as large-scale fading and are explained by the CE2R model as described in [11]. This reflection model describes the behavior of the of a received signal which is composed of two signals via superposition: The LOS signal and the signal reflected off the ground. In our case, this composed signal (mostly) defines the dominant component as introduced above. The theoretical signal power based on the CE2R model is also given in Fig. 13. Apparently, the model and the measured received power match quite well. We ascribe the deviations to varying permittivities at the reflection point and a varying relative altitude which is not considered in the given model. The CE2R model can be applied only under the condition that the LOS path and the ground wave path are not resolvable at the receiver, thus that their path lengths differ by less than Δr_{min}. The authors have verified that this condition is fulfilled for the geometry observed in Fig. 13.

D. Go-around

Fig. 15 shows the received power during eleven go-arounds (see Section V) flown at different altitudes above the runway of the EDMO airport.

The displayed parts of the go-around all have a "U"-shaped flight altitude profile, where the bottom part is flown with different altitudes over the runway ("runway part") as can be seen in Fig. 15a. During the runway part, the roll, pitch and yaw angles of the aircraft were all kept around 0°. The received power is comparatively strong ($> -5\,\mathrm{dB}$), except for two sections ("drop section") labeled A and B where the received power partially drops down to $-22\,\mathrm{dB}$.

The position of these drop sections with respect to the transmitter can be identified better in Fig. 15b, where the received power is plotted in dependency on the azimuth angle φ and the polar angle θ according to the East-North-Up (ENU) coordinate system as defined in Appendix B.

The dependency of the received power on the azimuth angle is clearly visible. The two drop sections A and B are highlighted in both plots and are found to be in the range of $89° < \varphi < 94°$ and $114° < \varphi < 122°$, respectively. Although

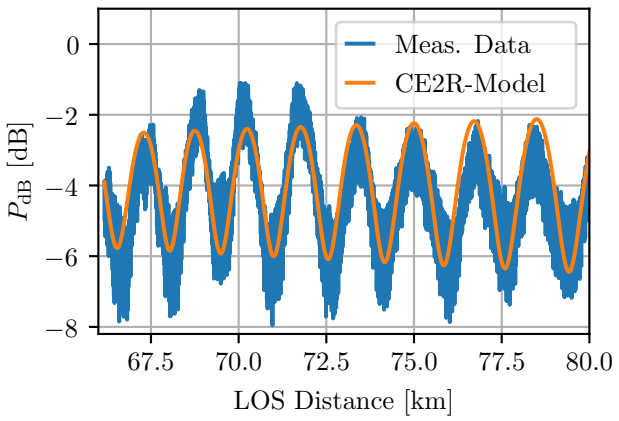

Fig. 13. Received power during en-route vs. the distance between the transmitting and the receiving antenna. The aircraft is following a radial course away from the transmitter. Both the received power computed from the measurement data and the result of the Curved-Earth Two-Ray (CE2R) model are plotted.

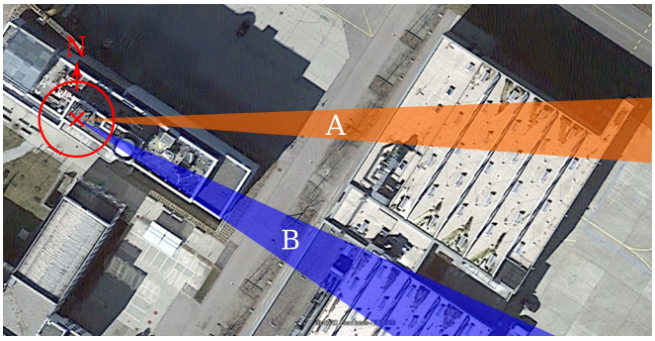

Fig. 14. Bird view of the transmitter (marked by a red cross) and its immediate environment. A and B mark the angle ranges where significant drops in received power are observed during go-arounds. Please note that neither the roof northwest of the transmitter nor the construction crane north of the transmitter were present during the measurement flights. Background image: ©2020 GeoBasis-DE/BKG, Google Earth

the antenna pattern of the transmitter is not considered during data processing, we do not affiliate these significant drops to the antenna, as we do not see a similar power drop at similar azimuth angles in other flight scenarios. As the go-arounds were flown along both directions of the runway, we also consider it as unlikely that the drops can be explained by the receiver's antenna pattern. An analysis of the NED angles and the aircraft's architecture shows that we can also rule out airframe shadowing as the reason for the drops in received power. Therefore, we assume the power drops in A and B are caused by obstacles between the transmitter and the receiver that cause interfering rays (non-resolvable scatter components) that degrade the computed received power of the dominant component.

Let us first have a look on the situation in drop zone A: Fig. 14 shows that parts of the roof of a hangar building intersect with the ground projection of the LOS path for the corresponding angle range of $89° < \varphi < 94°$. The authors have verified that this roof does not block LOS path between the transmitter and the receiver for any of the flights observed here. We therefore assume, that these drops are caused by non-resolvable signal components reflected off this roof and reflected off obstacles located on this roof. Apparently, these components are contributing to the dominant component destructively. The condition for a non-resolvable signal path is that the distance between the length of the LOS path and the length of the reflected path is less than Δr_{min}. Considering the location and height of the hangar building, we were able to find reflection points on this roof fulfilling this condition for the specific angle range for all flights. Drop zone A is bounded by higher obstacles located on the roof blocking the path of the reflected signals for greater values of φ as it can be verified in Fig. 14.

For drop zone B we have another explanation of the low received power: Fig. 14 reveals that a small radome is located about $15\,\mathrm{m}$ southeast of the transmitter. The radome is not that high that it blocks the LOS path for any of the flights, however, its top is high enough to disrupt the estimated first Fresnel Zone of the link between the transmitter and the receiver at least partially for $114° < \varphi < 122°$. We assume that the radome, therefore, causes the recorded power drops in zone B.

We understand these findings as a hint that the immediate environment of the ground antenna has a strong impact on the resulting channel conditions, especially in critical flight maneuvers like go-arounds. We therefore suggest to carefully choose the ground antenna's location.

VII. Amplitude Distribution

In this section, we analyze the distribution of the received amplitudes x for different flight scenarios. In a first step, we apply a Gaussian Kernel Density Estimation (KDE) [23] to visualize the respective amplitude distributions. We then use a Downhill-Simplex based algorithm to find the maximum likelihood parameter estimates for a Rice and a Nakagami PDF which best fit the given data. Both the Rice and the Nakagami distributions are common approaches to model the distribution of received amplitudes when transmitted over a wireless channel. Finally, we use the Mean Squared Error (MSE) between the KDE and the two estimated Probability Density Functions (PDFs) to determine which of the two distributions provides the better fit for the corresponding data set.Although the Nakagami distribution is a more flexible approach providing more degrees of freedom, we observed that it does not substantially outperform the Rice fit in any of the scenarios investigated. We provide both solutions to the reader since the Rice distribution is less complex and its fitting lead, in contrast to the Nakagami fit, to a numerically stable solution for all of the investigated scenarios.

The Nakagami distribution is given by

$$f_N(x,\mu,\beta,m) = \frac{2m^m}{\Gamma(m)}\xi(x)^{2m-1}\exp\Big\{-m\xi(x)^2\Big\}, \quad \text{with}$$
$$\xi(x) = (x-\mu)/\beta, \tag{12}$$

where β is a scaling factor, μ defines the PDF's location, $\Gamma(.)$ denotes the Gamma distribution, and m denotes the shape parameter.

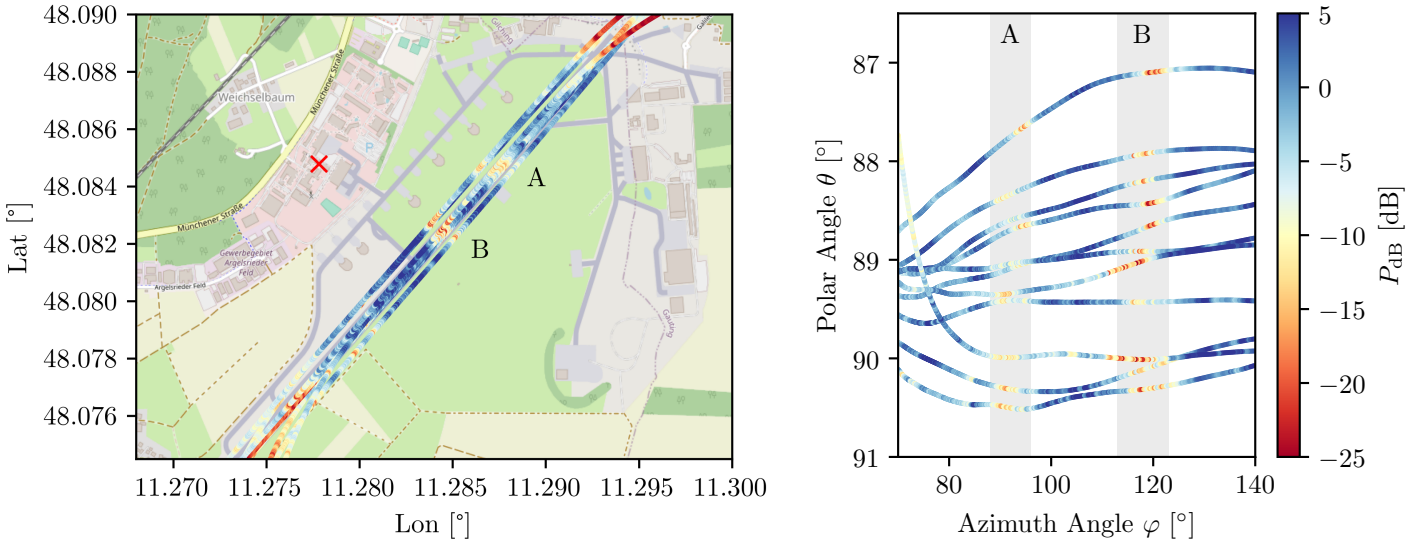

(a) Map of the runway, some airport buildings, and the transmitter (red cross)

(b) Dependency on ENU angles (see Appendix B)

Fig. 15. Received power during eleven go-arounds recorded during all four flights. The two "drop sections" are marked with A and B, respectively. While A shows not that significant drops, the received power in B drops by up to 22 dB.

The PDF of the (standardized, i.e. $\sigma = 1$) Rice distribution is given by

$$f_R(x, \mu, \beta, b) = \frac{\xi(x)}{\beta} \exp\left\{ -\frac{\xi(x)^2 + b^2}{2} \right\} I_0(\xi(x) b), \quad \text{with}$$
$$\xi(x) = (x - \mu)/\beta, \tag{13}$$

where β and μ again define the distribution's scale and location, respectively, $I_0(.)$ denotes the modified Bessel function of the 0-th order, and b is the shape parameter. Following the definition above, the well-known K factor describing the power ratio of the LOS component and the multipath components of the Rice PDF is given by $K = b^2$. For $b \to 0$, the Rice distribution tends to the Rayleigh distribution.

The estimated parameters for the amplitude distributions during the scenarios investigated in the following are given in Table III. The table provides also an estimate of the presence of an unblocked LOS between the transmitter and the receiver (0 % corresponding to pure non-LOS, 100 % corresponding to pure LOS). These estimates were calculated based on GNSS and IMU data similar to the approach described in Section VI-A.

Please note that the following analysis was performed on the range between the 5th and the 95th percentile of the data to reduce the effect of outliers. The effect of the FSPL was compensated according to (11).

A. Taxiing

The distribution of the received amplitudes during taxiing at the apron is given in Fig. 16. Both the KDE and the fitted Rician and Nakagami PDF are plotted. The MSE of the Nakagami approach is slightly better than the Rician approach, however, the deviation is minimal. Comparing the determined fits to the KDE visually suggest, that the underlying channel

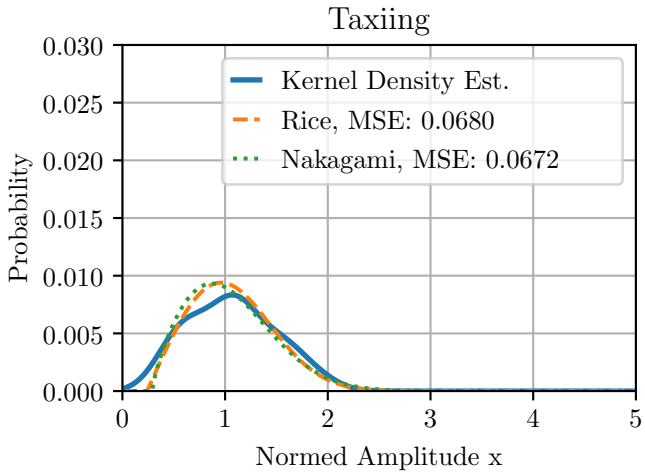

Fig. 16. Distribution of the dominant component's amplitudes during taxiing: Kernel Density Estimation (KDE) based estimation and result of a fitted Rice and Nakagami PDF (parameters given in Table III).

observed during the measurement cannot be perfectly represented by just a single PDF. We assume this is caused by changing channel conditions as the aircraft is moving on the apron.

The corresponding data in Table III shows that no LOS was present during the recording of the data. Nevertheless, in contrast to the takeoff scenario discussed below, the distribution does not tend towards a Rayleigh distribution. We explain this by the continuous presence of the ground during taxiing that acts as a reflector.

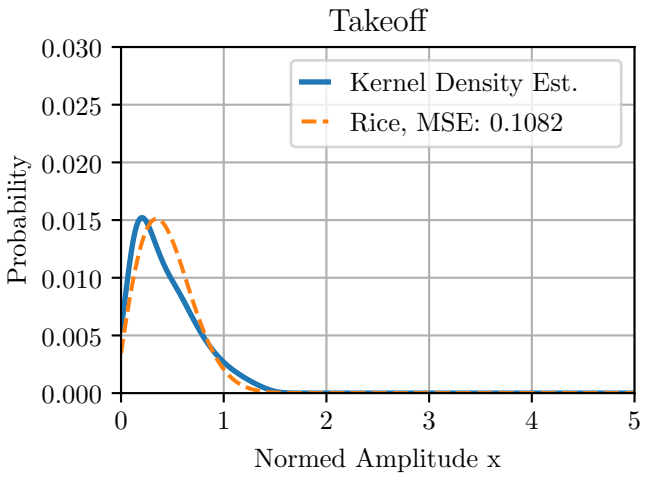

Fig. 17. Distribution of the dominant component's amplitudes during takeoff: Kernel Density Estimation (KDE) based estimation and result of a fitted Rice PDF (parameters given in Table III).

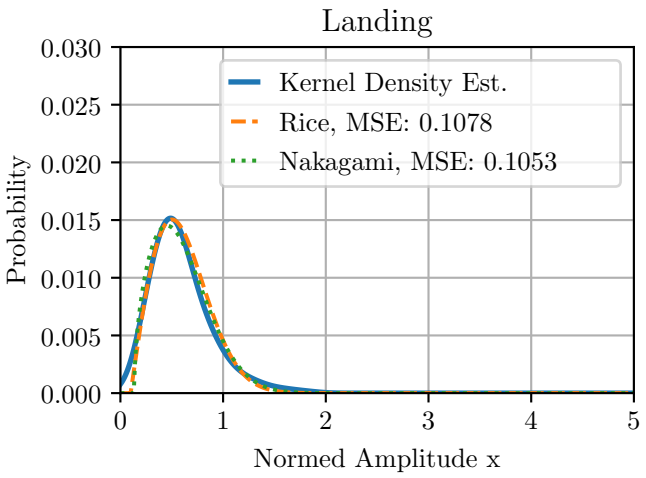

Fig. 18. Distribution of the dominant component's amplitudes during landing: Kernel Density Estimation (KDE) based estimation and result of a fitted Rice and Nakagami PDF (parameters given in Table III).

B. Takeoff and Landing

The distribution of the received amplitudes during takeoff of all four flights is given in Fig. 17. The figure shows both the KDE and the PDF of a Rice distribution fitted to the underlying data[12].

According to the corresponding entry in Table III, the shape parameter b of the Rician PDF is close to zero. As mentioned above, this lets the Rician distribution tend towards a Rayleigh distribution – a common approach to model a non-LOS scenario in wireless communications. Therefore, we state that the receiving antenna at the aircraft is shadowed by the airframe during takeoff for practically all the time. This assumption is supported by the estimated LOS presence of 0 %. It can be understood when the geometry of the position of the transmitter, the runway, the starting direction, and the positive pitch angle (i.e. "nose up") of the aircraft during climbing is considered and also matches the findings from Section VI-B.

The amplitude distribution during landing ("final approach") of all four flights is presented in Fig. 18. Both the KDE and the Rice and Nakagami PDF fits are plotted; the latter shows a slightly lower MSE.

The amplitude distribution parameters again reveal a mostly blocked LOS path, however, not as consequent as for the takeoff scenario. In contrast to the takeoff scenario, the aircraft's airframe is not consequently blocking the LOS path during its approach to the runway: It is descending and heading towards the transmitter while still having a mostly non-negative pitch angle.

C. En-route (ENR) - Circles

Figs. 19 and 20 show the amplitude distribution during parts of flight I ("circular patterns"). The circles are 23 km ("small") and 62 km ("large") in diameter, respectively, and were flown at different altitudes: 3.2 km ("low") and 10.9 km ("high"). The corresponding flight track is highlighted in a miniaturized map of flight I (compare Fig. 10a) in each plot.

Fig. 19 compares the distributions of the amplitudes received during the track following the small and the large circle at the low flight altitude. Since the transmitter is located in the center of both circles, the larger diameter corresponds to a larger LOS distance, while the flight altitude above ground is approximately the same. The circular shape of the pattern results in a more or less constant polar angle as defined in Appendix B for each circle. The different circle diameters lead to a significant difference in the resulting polar angle: While the mean polar angle in Fig. 19a is $\bar{\theta} \approx 76°$, it is $\bar{\theta} \approx 84°$ in Fig. 19b. This leads to different conditions of the wireless propagation channel, since the probability of a blocked LOS path is higher in case of a greater $\bar{\theta}$. A visual comparison, and the comparison of the corresponding entries in Table III, show that the differences in the channel conditions are also observable in the amplitude distributions. Apparently, the polar angle has a strong influence on the resulting amplitude distribution at the receiver. The distribution parameters from Table III suggest that the scenario in Fig. 19b tends closer towards a non-LOS scenario than the scenario presented in Fig. 19a. This statement is supported by the estimated presence of LOS for the corresponding scenarios (56 % and 77 %, respectively).

Fig. 20 shows a similar flight pattern as described in the previous paragraph, however, at a significantly higher flight altitude of about 10.9 km. This results in smaller polar angles compared to the low flight altitude: $\bar{\theta} \approx 49°$ and $\bar{\theta} \approx 71°$ for the small and the large circle, respectively. The impact on the amplitude distributions is also clearly visible: Both Fig. 20a and Fig. 20b show a LOS scenario. Please also note, that the scenarios in Fig. 19a and Fig. 20b, where the mean polar angles are in a similar range, show comparable amplitude distributions.

[12]As the applied optimization algorithm was unable to find an acceptable solution for the Nakagami distribution, we dropped this approach for the takeoff scenario.

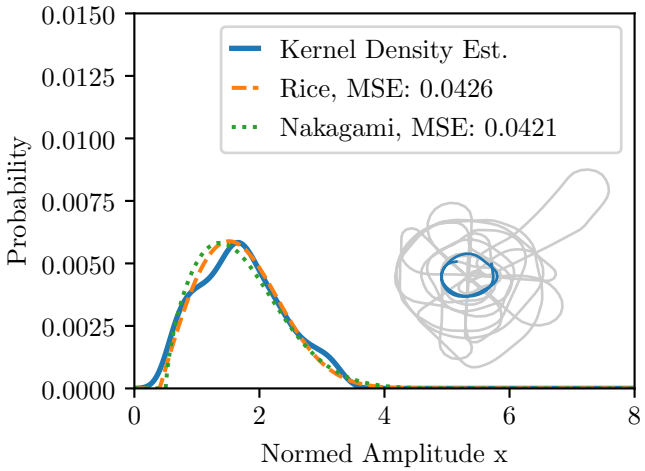

(a) Circle diameter of roughly 23 km

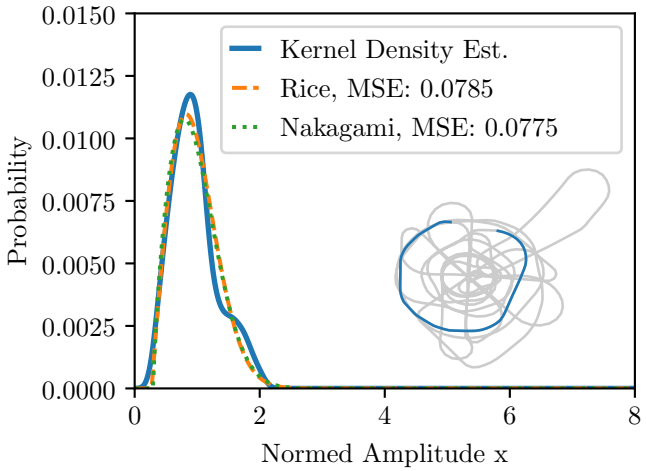

(b) Circle diameter of roughly 62 km

Fig. 19. Kernel Density Estimation (KDE) and fitted Rician and Nakagami Probability Density Function (PDF) of the distribution of the dominant component's amplitudes during en-route for a circular flight pattern highlighted in the light grey map at a flight altitude of roughly 3.2 km. The parameters for the corresponding fits are given in Table III.

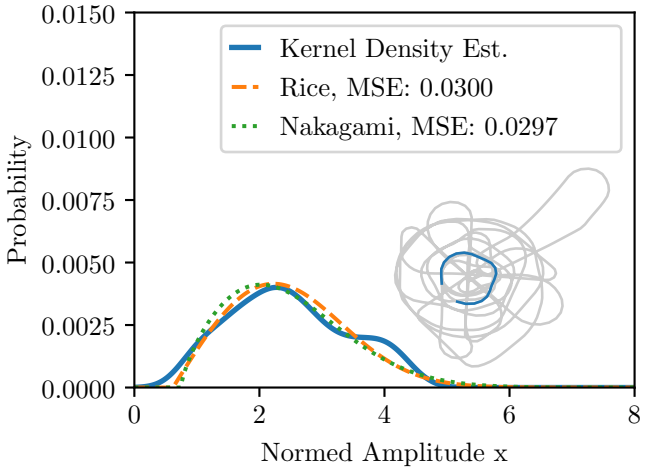

(a) Circle diameter of roughly 23 km

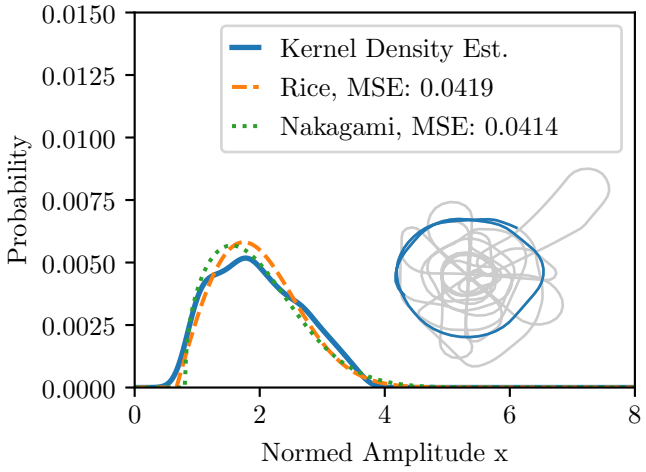

(b) Circle diameter of roughly 62 km

Fig. 20. Kernel Density Estimation (KDE) and fitted Rician and Nakagami Probability Density Function (PDF) of the distribution of the dominant component's amplitudes during en-route for a circular flight pattern highlighted in the light grey map at a flight altitude of roughly 10.9 km. The parameters for the corresponding fits are given in Table III.

D. En-route (ENR) - Squares

Fig. 21 shows the amplitude distribution during parts of flight III ("square-type patterns") at a flight altitude of roughly 3.2 km[13]. While a small square-type pattern with an edge length of roughly 30 km is flown in Fig. 21a, a larger square-type pattern with an edge length of about 52 km is flown in Fig. 21b. Although the flight altitude is kept the same during both flights, the non-circular shape of the flight tracks result in a varying polar angle. However, the average polar angle for the scenario presented in Fig. 21a is smaller than the average polar angle in the scenario presented in Fig. 21b for the same reasons explained in the previous section.

Similar to the circular pattern, the probability of receiving larger amplitudes for the square-type flight patterns is larger for the smaller square (Fig. 21a) than for the greater square (Fig. 21b). It is also interesting to see that even in the case of the large square, the distribution shows a higher probability for larger amplitudes compared to the large circular pattern at the same flight altitude (Fig. 19b). On the one hand, the average polar angle in the large square-type pattern is not as large as in the case of the large circular pattern. However, this might not be the only reason for the higher probability of receiving a larger amplitude compared to the circular pattern: The pilot of an aircraft flying a circle has to correct the aircraft's heading

[13]Please note that only the data recorded while flying along the actual edges of the square-type pattern is discussed here. The parts of the flight where the turns from one edge to the next were flown are skipped, since the channel conditions are not comparable to those during a flight along the edges.

continuously, which in practice impacts not only the yaw angle, but also the roll angle of the aircraft. Especially in case of a large polar angle, even these minor corrections increase the probability of a blocked LOS path. In contrast, no such continuous heading correction is necessary when flying along the edges of a square.

VIII. Conclusion and Outlook

In this paper we have described a flight campaign investigating the physical properties of the C-band air-ground channel for different flight scenarios. We have furthermore presented first results of the evaluation of the recorded signal. The results presented here focus on the power of the dominant component and the amplitude distribution. We have investigated the received power and the received signal amplitudes and showed their behavior and distribution, respectively. Comparing these results within the different flight scenarios showed significant distinctions. We understand these findings as a motivation to develop an adjustable channel model for the different flight scenarios, as we do not think that the detected distinctions can be covered by just one simple model.

As a next step we will focus on the detection and tracking of the resolvable multipath components during the different flight scenarios.

Acknowledgment

We would like to thank all people involved in the ALPS measurement campaign.

Appendix

A. Power Delay Profile (PDP)

The discrete coherent Power Delay Profile function $\mathrm{PDP}_{\mathrm{coh}} : \mathbb{C}^{BN} \times \mathbb{C}^{N} \mapsto \mathbb{R}^{f_{\mathrm{ups}}N}$ of a vector $\boldsymbol{y} \in \mathbb{C}^{BN}$ w. r. t. the reference signal $\boldsymbol{x}_{\mathrm{ref}} \in \mathbb{C}^{N}$ is computed as follows:

- To simplify the following processing steps, the matrix $\boldsymbol{Y} \in \mathbb{C}^{N \times B}$ is defined, whose (m, n)-th element is set to $\boldsymbol{y}[m + nN]$.
- An FFT of length N is performed along each column of $\boldsymbol{Y}$: $\boldsymbol{Y}'_i = \mathfrak{F}\mathfrak{F}\mathfrak{T}_{N,\downarrow}\{\boldsymbol{Y}\}$.
- The matrix $\boldsymbol{X}_{\mathrm{ref}} \in \mathbb{C}^{N \times B}$ is created, whose (m, n)-th element is set to $\boldsymbol{x}_{\mathrm{ref}}[m]\ \forall n \in \{0, 1, ..., B-1\}$ and the FFT is computed: $\boldsymbol{X}'_{\mathrm{ref}} := \mathfrak{F}\mathfrak{F}\mathfrak{T}_{N,\downarrow}\{\boldsymbol{X}_{\mathrm{ref}}\}$.
- An element-wise multiplication $\boldsymbol{K}' := \boldsymbol{Y}' \cdot \boldsymbol{X}'_{\mathrm{ref}}$ is performed, and zero-padding is applied by expanding $\boldsymbol{K}'$ by $(f_{\mathrm{ups}} - 1)N$ rows of zeros resulting in $\boldsymbol{K}'_{\mathrm{pad}}$.
- An Inverse Fast Fourier Transform (IFFT) is performed: $\boldsymbol{K} := \mathfrak{I}\mathfrak{F}\mathfrak{F}\mathfrak{T}_{f_{\mathrm{ups}}N,\downarrow}\{\boldsymbol{K}'_{\mathrm{pad}}\}$.
- The absolute value of the mean along all rows of $\boldsymbol{K}$ is computed: $\boldsymbol{a} := \left|\mathrm{MEAN}_{\rightarrow}\{\boldsymbol{K}\}\right|$.
- The result is converted to dB-scale: $\boldsymbol{a}_{\mathrm{dB}} = 20 \log_{10}\{\boldsymbol{a}\}$

B. Transmitter Centered Coordinate System

We first define a Cartesian coordinate system with the transmitting antenna in its origin: an East-North-Up (ENU) system, where the x-axis shows into the *East* direction, the y-axis shows into the *North* direction, and the z-axis shows *Up* into the sky. More precise: the negative z-axis shows into the center of gravity of the Earth according to the World Geodetic System 1984 (WGS84). We then define the ENU azimuth angle $\varphi_{\mathrm{ENU}} \in [0°, 360°)$ as the clockwise rotation around the z-axis where $\varphi_{\mathrm{ENU}} = 0°$ indicates the north direction. The polar angle $\theta_{\mathrm{ENU}} \in [0°, 180°)$ is the angle between the LOS and the z-axis, such that all points with $\theta_{\mathrm{ENU}} = 90°$ lie in the xy-plane.

C. Receiver Centered Coordinate System

The North-East-Down (NED) coordinate system is a Cartesian coordinate system fixed to the aircraft with the receiving antenna in its origin. The axes are defined as shown in Fig. 6: *North* (x-axis) is heading into the direction of the aircraft's nose, i.e. towards the viewer, which usually corresponds to the flight direction. *East* (y-axis) is heading to the left of the figure, which corresponds to starboard during flight. *Down* (z-axis) is heading downwards, usually towards the ground. Corresponding to the ENU system, we define the angles as follows: The azimuth angle $\varphi_{\mathrm{NED}} \in [0°, 360°)$ is the positive rotation around the z-axis where $\varphi_{\mathrm{NED}} = 0°$ corresponds to the x-axis. We define the polar angle $\theta_{\mathrm{NED}} \in [0°, 180°)$ as the angle between the LOS and the z-axis, where $\theta_{\mathrm{NED}} = 0°$ equals the z-axis and all points with $\theta_{\mathrm{NED}} = 90°$ lie in the xy-plane. The transmitter's position given in spherical NED coordinates allows a straight forward analysis whether the LOS connection is blocked by the airframe or not.

We can use the NED system to define the aircraft's rotation axes: *Roll* is a positive rotation around the x-axis. *Pitch* is a positive rotation around the y-axis. *Yaw* is a positive rotation around the z-axis.

References

[1] "Ip/14/384: European commission calls for tough standards to regulate civil drones," 2014. [Online]. Available: http://europa.eu/rapid/press-release_IP-14-384_en.htm

[2] M. Schnell, U. Epple, D. Shutin, and N. Schneckenburger, "LDACS: future aeronautical communications for air-traffic management," *IEEE Communications Magazine*, vol. 52, no. 5, pp. 104–110, May 2014.

[3] T. Graupl, M. Ehammer, and C.-H. Rokitansky, "L-DACS 1 data link layer design and performance," in *Integrated Communications, Navigation and Surveillance Conference, 2009. ICNS'09.* IEEE, 2009, pp. 1–12.

[4] "Report ITU-R M.2171," ITU, 12 2009.

[5] R. SC-228, "RTCA paper no. 075-14/pmc-1201: Command and control (C2) data link white paper," 2014.

[6] "Report ITU-R M.2205," ITU, 11 2010.

[7] D. M. Mielke, "C-band digital aeronautical communication for unmanned aircraft systems," in *2017 IEEE/AIAA 36th Digital Avionics Systems Conference (DASC)*, Sep. 2017, pp. 1–7.

[8] D. M. Mielke, "Frame structure of the C-band digital aeronautical communications system," in *2018 Integrated Communications, Navigation, Surveillance Conference (ICNS)*, April 2018, pp. 2C4–1–2C4–12.

[9] E. Haas, "Aeronautical channel modeling," *IEEE Transactions on Vehicular Technology*, vol. 51, no. 2, pp. 254–264, Mar 2002.

[10] P. Pulini, S. Plass, L. Taponecco, M. Morelli, and L. Sanguinetti, "Aeromacs evolution - extension to landing, take-off, and approach phases," in *2013 Integrated Communications, Navigation and Surveillance Conference (ICNS)*, April 2013, pp. 1–14.

[11] D. W. Matolak and R. Sun, "Air-ground channel characterization for unmanned aircraft systems - part I: Methods, measurements, and models for over-water settings," *IEEE Transactions on Vehicular Technology*, vol. 66, no. 1, pp. 26–44, Jan 2017.

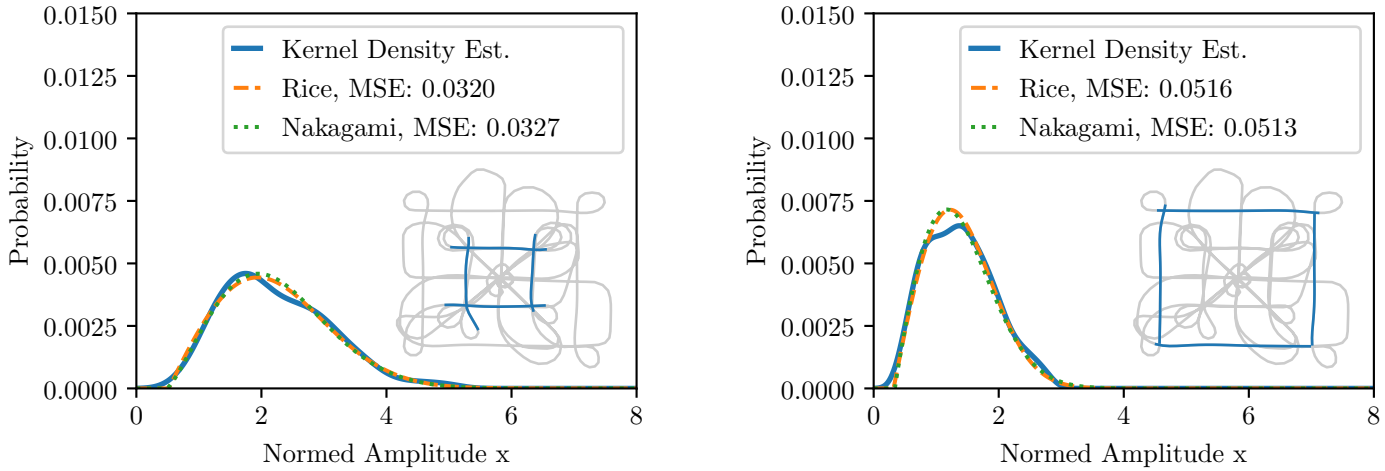

(a) Edge length of roughly 30 km

(b) Edge length of roughly 52 km

Fig. 21. Kernel Density Estimation (KDE) and fitted Rician and Nakagami Probability Density Function (PDF) of the distribution of the dominant component's amplitudes during en-route for a square-type flight pattern highlighted in the light grey map at a flight altitude of roughly 3.2 km. The parameters for the corresponding fits are given in Table III.

TABLE III
RICE AND NAKAGAMI DISTRIBUTION PARAMETERS FOR THE DISTRIBUTION OF THE DOMINANT COMPONENT'S AMPLITUDES FOR SEVERAL FLIGHT SCENARIOS INCLUDING INFORMATION ON THE RESPECTIVE PRESENCE OF LOS

Scenario	Figure	LOS present	Best distribution fit	Rice			Nakagami		
				Location μ	Scale β	Shape b	Location μ	Scale β	Shape m
Taxiing	Fig. 16	0 %	Nakagami	0.2409	0.5110	1.1310	0.2890	0.8826	0.8914
Takeoff	Fig. 17	0 %	Rice	−0.0558	0.4014	0.0004	-	-	-
Landing	Fig. 18	81 %	Nakagami	0.0994	0.4031	0.0006	0.1343	0.5401	0.7695
ENR Small Circle @ 3.2km	Fig. 19a	77 %	Nakagami	0.4036	0.8412	1.0166	0.5049	1.3757	0.8239
ENR Large Circle @ 3.2km	Fig. 19b	56 %	Nakagami	0.2711	0.5531	0.0011	0.2953	0.7610	0.8823
ENR Small Circle @ 10.9km	Fig. 20a	100 %	Nakagami	0.6175	1.1682	1.0936	0.7456	1.9748	0.8611
ENR Large Circle @ 10.9km	Fig. 20b	94 %	Nakagami	0.6679	0.9065	0.8050	0.8084	1.3525	0.7144
ENR Small Square @ 3.2km	Fig. 21a	98 %	Rice	0.5178	1.1683	0.8588	0.4891	1.9585	1.1243
ENR Large Square @ 3.2km	Fig. 21b	97 %	Nakagami	0.3181	0.7016	0.9749	0.3392	1.1864	0.9738

[12] R. Sun and D. W. Matolak, "Air-ground channel characterization for unmanned aircraft systems - part II: Hilly and mountainous settings," *IEEE Transactions on Vehicular Technology*, vol. 66, no. 3, pp. 1913–1925, March 2017.

[13] D. W. Matolak and R. Sun, "Airground channel characterization for unmanned aircraft systemspart III: The suburban and near-urban environments," *IEEE Transactions on Vehicular Technology*, vol. 66, no. 8, pp. 6607–6618, 2017.

[14] R. Sun, D. W. Matolak, and W. Rayess, "Air-ground channel characterization for unmanned aircraft systemspart IV: Airframe shadowing," *IEEE Transactions on Vehicular Technology*, vol. 66, no. 9, pp. 7643–7652, 2017.

[15] N. Schneckenburger, T. Jost, D. Shutin, M. Walter, T. Thiasiriphet, M. Schnell, and U. Fiebig, "Measurement of the l-band air-to-ground channel for positioning applications," *IEEE Transactions on Aerospace and Electronic Systems*, vol. 52, no. 5, pp. 2281–2297, 2016.

[16] D. M. Mielke and N. Schneckenburger, "Towards a data link for unmanned aviation: DLR flight measurement campaign for C2 data link development," in *2019 Integrated Communications, Navigation and Surveillance Conference (ICNS)*, April 2019, pp. 1–8.

[17] S. Boyd, "Multitone signals with low crest factor," *IEEE Transactions on Circuits and Systems*, vol. 33, no. 10, pp. 1018–1022, October 1986.

[18] *SESAR2020 PJ14-02-01 -LDACS A/G Specification*, SESAR Std., Aug. 2019. [Online]. Available: https://www.ldacs.com/wp-content/uploads/2013/12/SESAR2020_PJ14_D3_3_030_LDACS_AG_Specification_00_02_02-1_0.pdf

[19] *Aeronautical Telecommunications Annex 10, Vol. 3*, ICAO Std., Rev. 2, Jul. 2007.

[20] N. Schneckenburger, T. Jost, D. Shutin, M. Walter, G. del Galdo, and U. Fiebig, "Reflector localization for geometrical modeling the airground channel," *IEEE Transactions on Vehicular Technology*, vol. 67, no. 9, pp. 7994–8008, 2018.

[21] N. Schneckenburger, "A wide-band air-ground channel model," Ph.D. dissertation, University of Ilmenau, 2017.

[22] F. A. Administration, *Airplane Flying Handbook FAA-H-8083-3B*, United States Department of Transportation, P.O. Box 25082, Oklahoma City, OK 73125, 2016.

[23] T. Ledl, "Kernel density estimation: Theory and application indiscriminant analysis," *Austrian Journal of Statistics*, vol. 33, no. 3, pp. 267–279, 2004.